
Picosecond Thermodynamics in Underdense Plasmas Measured with Thomson Scattering

Endeavors to engineer plasmas for a number of applications rely critically on plasma conditions. Optimizing plasma devices, including laser amplifiers,^{1–3} laser compressors,⁴ wave plates,^{5,6} polarizers,^{7,8} *Q* plates,⁹ particle accelerators,^{10,11} photon accelerators,¹² high-order frequency conversion,^{13,14} and photon–electron light sources,^{15,16} require an accurate knowledge of plasma density and temperature dynamics. In these systems, the electromagnetic fields generate dynamic plasma conditions that typically evolve over the initial 50 ps. During the rise of a high-intensity laser pulse, the photoionized electrons are liberated with minimal kinetic energy, resulting in an initially cold plasma. The energy supplied to the electrons by the electromagnetic field through inverse bremsstrahlung causes the temperature to rise rapidly until the collisionality of the plasma reduces the heating rate to a level comparable to the cooling mechanisms. Measurements of these early plasma dynamics on application-relevant times scales have been previously unattainable.

Optical Thomson scattering is a powerful diagnostic that can accurately measure plasma conditions,^{17–23} but it has had limited temporal resolution (>50 ps) (Ref. 24). Experiments have used ultrashort (<1-ps) Thomson-scattering probe beams²⁰ to improve the temporal resolution, but these studies were focused on measurements of nonequilibrium electron plasma waves (EPW's) and the large bandwidth contained in the ultrashort Thomson-scattering probe beam prevented the measurement of the plasma conditions. Furthermore, during plasma formation, the collisional damping dominates over the Landau damping of EPW's and a collisional theory is required to accurately model the Thomson-scattering spectrum. Thomson-scattering measurements of collisional EPW's have been limited to non-ideal plasmas in which the short-range coulombic interaction between charges determines the dynamics as opposed to the collective behavior.^{25–27} In these nonideal plasmas, theories have been developed to interpret the Thomson-scattering spectrum.^{28,29} The standard computationally efficient approach to include collisions is to use the approximate Bhatnagar–Gross–Krook (BGK) collision operator,^{30,31} but recently the more-accurate linearized Vlasov–Fokker–Planck (VFP) equation

was presented to account for collisions in calculations of the Thomson-scattering spectrum.³²

In this article, we report the first observation of the effects of collisions on electron plasma waves in an ideal plasma. The measurements were obtained by an ultrafast high-throughput spectrometer that provided unprecedented temporal resolution of the EPW Thomson-scattering spectra. These spectra provided a measurement of collisional EPW's that were modeled to extract the picosecond evolution of the electron temperature and density. The standard treatment of an ideal plasma is to assume that Landau damping is the only active damping mechanism; however, the measurements of the initial plasma demonstrated that the EPW damping was dominated by collisions. The hydrogen gas was ionized at an intensity near 10^{14} W/cm², where the initial electron plasma temperature and density were measured to be 3 eV and 8.40×10^{18} cm⁻³, respectively. Over the first 18 ps, the plasma temperature increased modestly (16 eV) as the plasma density became fully ionized (1.07×10^{19} cm³) and then rapidly increased to a saturated level of 93 eV over the next 20 ps. For temperatures below 45 eV, a collisional model was required to reproduce the measured spectrum. For the most-collisional conditions, the VFP-based scattering model shows that the BGK model significantly overestimates the effects of collisions, leading to an overestimation of the electron temperature by 50%.

The experiments were conducted on LLE's Multi-Terawatt (MTW) Laser System.³³ The 1054-nm pump laser irradiated a 4-mm-long hydrogen gas cell [Fig. 156.33(a)] at a molecular density of $\sim 5 \times 10^{18}$ cm⁻³ with a 1.4-J, 60-ps full-width-at-half-maximum (FWHM) square pulse (~ 5 -ps rise time). The pump beam was focused to a vacuum intensity of $\sim 3 \times 10^{14}$ W/cm² at the center of the gas cell by an *f*/25 spherical mirror. A fraction of the pump beam was frequency doubled (500 mJ) and co-propagated with the pump beam.

The $\lambda = 526.5$ -nm light, scattered from a $60\text{-}\mu\text{m} \times 60\text{-}\mu\text{m} \times 30\text{-}\mu\text{m}$ volume at the center of the gas cell, was collected and collimated by an *f*/2.4 achromatic lens located 90° from the

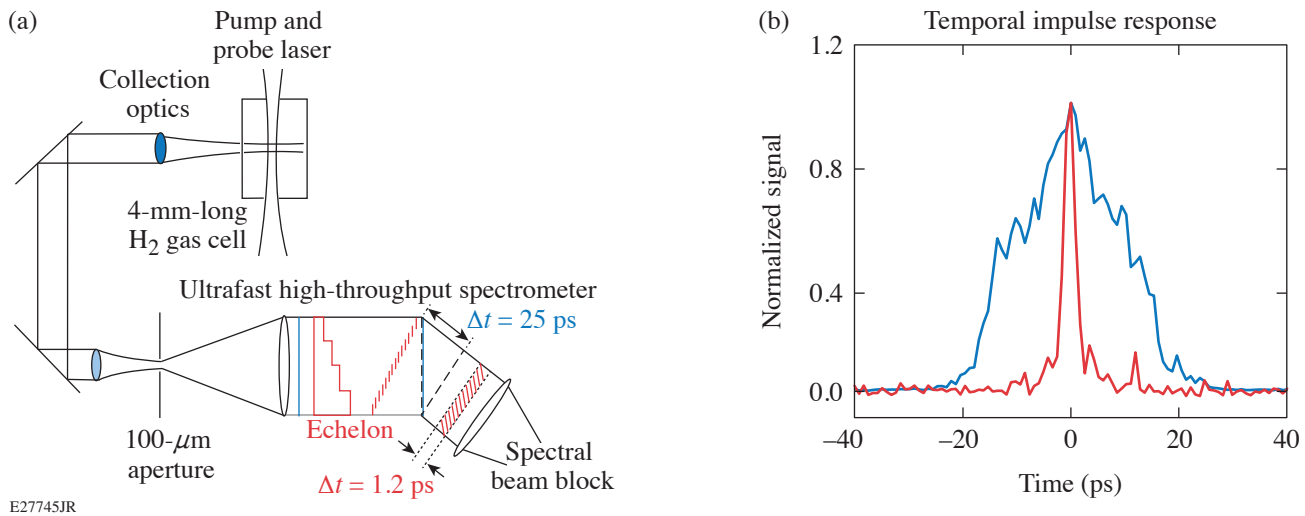


Figure 156.33

(a) A schematic of the experimental setup. (b) The measured temporal instrument response function with (red curve) and without (blue curve) the echelon installed. For schematic purposes, a transmission echelon is shown.

laser beam's propagation axis. The collected light was focused with an $f/4$ achromatic lens onto a 0.1-mm-diam aperture at the entrance of an $f/3$ pulse-front-tilt compensated spectrometer that was coupled to an ultrafast optical streak camera (ROSS P820).³⁴ The spectrometer collimated the light in a 100-mm-diam beam that was reflected from an echelon before propagating through a transmission grating and focused onto the streak camera slit. An ~ 200 - μm -wide beam block was positioned at the streak camera slit to eliminate light scattered around the probe's wavelength.

The spectral resolution in this system was dominated by the diameter of the aperture at the entrance of the spectrometer. To achieve the necessary spectral resolution for the measurements reported here, $\Delta\lambda = 1$ nm (FWHM), a linear grating density of 300 grooves/mm along with the 225-mm-focal-length spectrometer was used to spread the complete ~ 200 -nm Thomson-scattering spectrum across the detector. The combination of the beam diameter and the grating density results in a total number of grooves illuminated of $N = 3 \times 10^4$.

The pulse-front-tilt compensated spectrometer was invented to trade unutilized resolving power ($\lambda/\Delta\lambda = N$, $\Delta\lambda \simeq 0.02$ nm), with temporal resolution ($\Delta t \sim N\lambda/2c = 25$ ps), by using an echelon to separate the beam into $n = 20$ temporally delayed co-aligned beamlets. This reduced the pulse-front tilt of a conventional spectrometer with a streak camera limited spectral resolution of $\Delta\lambda = 1$ nm from ~ 25 ps to $\Delta t_c = \Delta t/n \sim 1.25$ ps, which is near the uncertainty principle limit ($\Delta t_{\text{limit}} = \lambda^2/2\Delta\lambda c \simeq 0.5$ ps), while maintaining 1-nm spectral resolu-

tion. Figure 156.33(b) compares measurements of the spectrometer–streak camera system resolution obtained with and without the echelon installed. The temporal resolution $\{G(t) = \exp[-4\ln(2)t^2/\tau^2]\}$ of the system was measured as a function of photoelectrons to account for space-charge broadening in the streak camera during the data analysis ($\tau = 2$ ps to 5 ps over the entire data range, where τ is the FWHM of the temporal impulse response of the spectrometer–streak camera system).

Figure 156.34 shows that the wavelength separation between the blue- and red-shifted spectral peaks increases for ~ 40 ps. This is a result of the increasing density and temperature: the wavelength separation between the features is proportional to the plasma frequency ($\sim \sqrt{\omega_{\text{pe}}^2 + 3v_{\text{th}}^2 k^2}$, where ω_{pe} is the plasma frequency and v_{th} is the electron thermal velocity). Late in time, this separation is relatively constant, indicating that the plasma has reached steady state. The streaked spectrometer integrated the scattered spectrum over the temporal instrument function ($\tau = 2$ ps); this was included in the spectrum calculations [Fig. 156.34(b)].

Figure 156.35 summarizes the picosecond plasma dynamics. The plasma was measured to initiate at a temperature of 3 eV and a density of $8.4 \times 10^{18} \text{ cm}^{-3}$. From this initial state, the plasma evolved to a steady-state temperature of 93 eV and a density of $1.07 \times 10^{19} \text{ cm}^{-3}$ over 40 ps. The plasma was calculated to be photoionized at an intensity near 10^{14} W/cm^2 , which corresponded to about half of the peak intensity, and occurred during the first few picoseconds of the rising laser pulse. This photoionized intensity threshold was confirmed by observ-

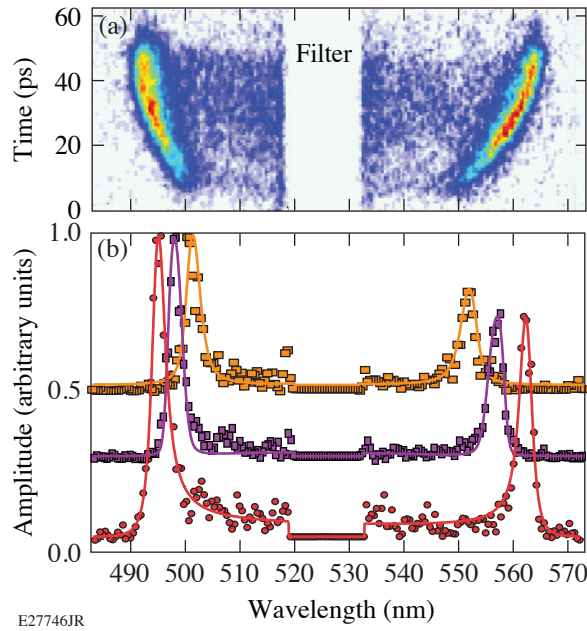


Figure 156.34

(a) The Thomson-scattering spectrum shows the temporal evolution of the electron plasma wave (EPW) features. Time zero coincides with the photoionization threshold laser intensity $\sim 10^{14}$ W/cm² of the heater beam. (b) The spectra at 9 ps (orange squares), 21 ps (purple squares), and 50 ps (red circles) were fit ($T_e^{9\text{ ps}} = 5$ eV, $n_e^{9\text{ ps}} = 8.9 \times 10^{18}$ cm⁻³, $T_e^{21\text{ ps}} = 26$ eV, $n_e^{21\text{ ps}} = 1.08 \times 10^{19}$ cm⁻³, $T_e^{50\text{ ps}} = 92$ eV, and $n_e^{50\text{ ps}} = 1.0 \times 10^{19}$ cm⁻³) with a scattering function that includes collisional effects through the Bhatnagar–Gross–Krook (BGK) model (solid curves). The two peaks in the scattered spectrum were normalized to match the calculated spectrum's amplitude.

ing the onset of the interferometry and Thomson-scattering signals. During the first 13 ps, the plasma temperature was moderated by the energy required to dissociate (4.52 eV) and ionize (13.6 eV) hydrogen, while also overcoming the cooling mechanisms of collisional excitation and ionization. Once the hydrogen was fully ionized, the plasma was heated by inverse bremsstrahlung absorption until an equilibrium was reached with the thermal conduction to the surrounding gas.

Figure 156.34(b) shows that the measured and simulated spectra are in excellent agreement. The temporal evolution was included in the calculated spectra by averaging the spectrum over the temporal instrument function,

$$P(t) = \sum_{i=t-\tau/2}^{t+\tau/2} G_i(t) P_i(\mathbf{k}, \omega),$$

where $P_i(\mathbf{k}, \omega)$ is the scattered power calculated with the plasma conditions at each time.³⁵ The Thomson-scattering spectra were initially fit to determine the electron temperature and density late in time ($t = 50$ ps) when there was no temporal

evolution [Fig. 156.34(b)]. The evolution of the plasma conditions was then determined by iteration. In the first iteration, the temperature evolution was calculated by assuming a constant density, which was found using the late time fit ($t = 50$ ps). In all following iterations, both the temperature and density evolution from the previous iteration were used. The process was repeated until the plasma conditions between subsequent iterations remained unchanged, which was achieved in the third iteration.

The spectra were fit using the Thomson-scattering spectrum³⁵

$$P(\mathbf{k}, \omega) = -\frac{A}{\omega} \left(1 + \frac{2\omega}{\omega_0} \right) \text{Im} \left[\frac{g(\mathbf{k}, \omega)}{\epsilon(\mathbf{k}, \omega)} \right], \quad (1)$$

where A is a normalization constant. For the most collisional conditions ($T_e < 18$ eV), a high-frequency (HF) approximation to the VFP dynamic structure factor [cf. Eqs. (55)–(57) from Ref. 32] was used, where $g(\mathbf{k}, \omega) = (J_N^N - \chi_e^{\text{HF}})$,

$$\epsilon^{\text{HF}}(\mathbf{k}, \omega) = 1 + \chi_e^{\text{HF}} = 1 + \left(1 + i\omega J_N^N / k^2 \lambda_D^2 \right)$$

is the plasma dielectric function,³⁶ J_N^N is the velocity moment of the zero-order harmonic from the solution to the complete

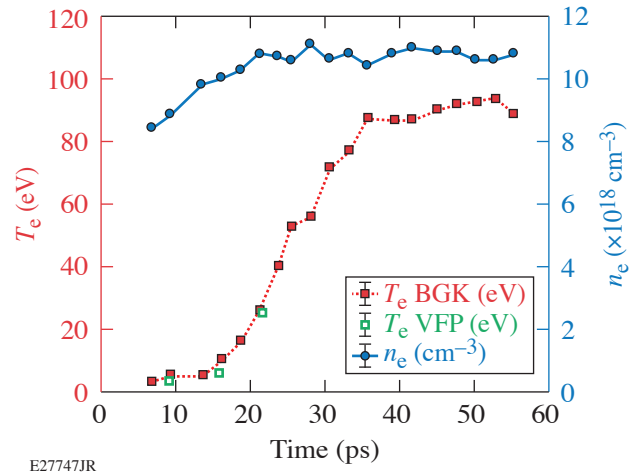
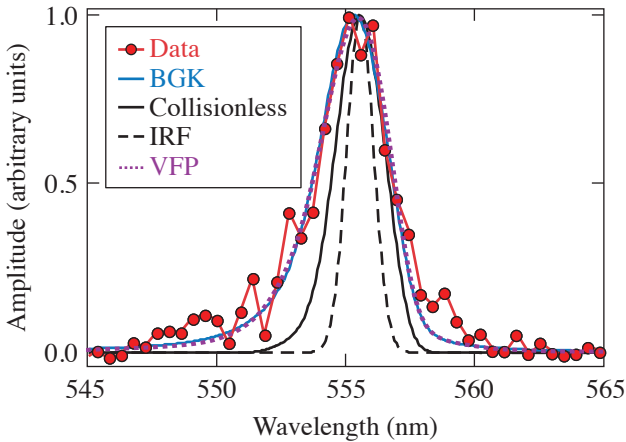


Figure 156.35

The measured electron temperature (red squares, left axis) and density (blue circles, right axis), determined by using the computationally efficient BGK approximation to calculate the spectrum, show the rapid evolution of the plasma. The parameters determined by the Vlasov–Fokker–Planck (VFP) collisional model are shown (green squares). The densities determined with the VFP model were identical to the densities (blue circles) determined when using the BGK model.

VFP equations,^{32,36} $\omega = \omega_0 - \omega_s$ is the plasma wave frequency, $\mathbf{k} = \mathbf{k}_0 - \mathbf{k}_s$ is the electron plasma wave vector, \mathbf{k}_0 is the Thomson-scattering probe wave vector, \mathbf{k}_s is the Thomson-scattered light wave vector, ω_0 is the Thomson-scattering probe frequency, ω_s is the Thomson-scattered light frequency, and λ_D is the Debye length.

Figure 156.36 shows that the Thomson-scattered spectrum calculated with the VFP model is an excellent fit to the measured spectrum. At these conditions, using the collisionless model resulted in a spectrum that was essentially a delta function and the experimental width was dominated by the temporal evolution in density and the instrument response function (IRF), which were narrower than the measurements. The Thomson-scattered spectra calculated with the BGK collisional model reproduced the measured scattering spectrum at all times, but in the most-collisional conditions, it overestimated the electron temperature by $\sim 50\%$ (Fig. 156.35). Detailed studies³¹ that have compared the BGK model to more complete theories based on the VFP kinetic equations have concluded that neglecting the electron–electron collisions and the crude approximation to the Coulomb collision operator in the BGK model leads to significant differences in the plasma response at Langmuir fluctuation frequencies.^{36,37} This leads to inaccurate calculations of the temperature when using the BGK model.



E27748JR

Figure 156.36

The measured spectrum (red circles) at 16 ps is compared to calculations that use a collisionless model (solid black curve, $T_e = 10$ eV, $n_e = 1.0 \times 10^{19} \text{ cm}^{-3}$), VFP collisional model (dotted purple curve, $T_e = 5$ eV, $n_e = 1.0 \times 10^{19} \text{ cm}^{-3}$), and BGK model (blue curve, $T_e = 10$ eV, $n_e = 1.0 \times 10^{19} \text{ cm}^{-3}$). The calculated spectra are convolved with the spectral instrument function (dashed black curve) and the spectra calculated with plasma conditions over the surrounding 2 ps.

The Thomson-scattering spectrum calculated with the BGK model^{32,35} used Eq. (1), where $g^{\text{BGK}}(\mathbf{k}, \omega) = -k^2 \lambda_D^2$ and the plasma dielectric function follows from the BGK model:^{30,31}

$$\epsilon^{\text{BGK}}(\mathbf{k}, \omega) = 1 + \frac{4\pi e^2}{m_e k^2} \times \int d^3v \frac{1}{\omega + i\nu_{ei}(v) - \mathbf{k} \cdot \mathbf{v}} \mathbf{k} \cdot \frac{\partial F_e}{\partial \mathbf{v}}. \quad (2)$$

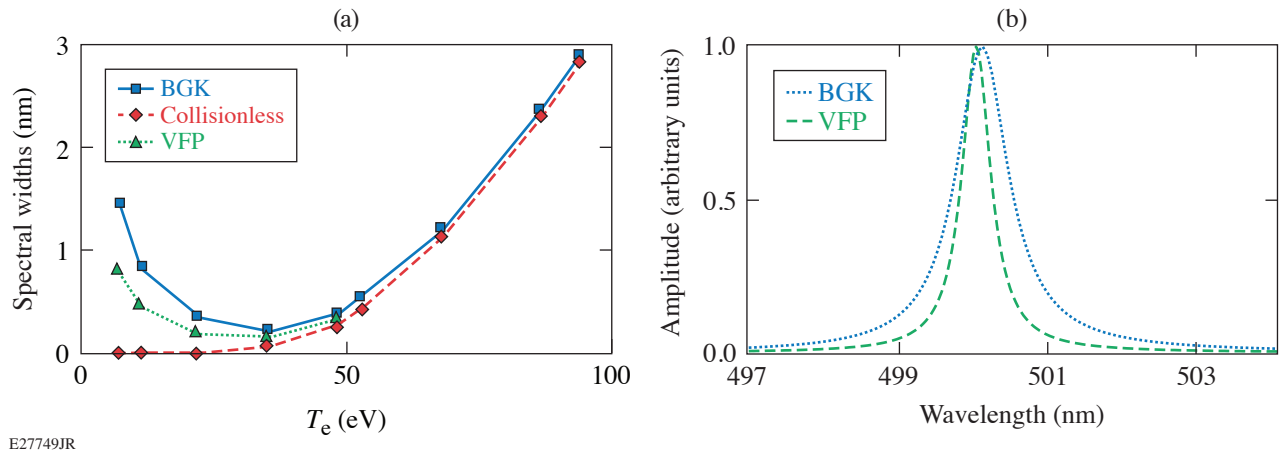
Here, the electron–ion collision frequency is given by $\nu_{ei} = 4\pi Z e^4 n_e \Lambda_{ei} / m_e^2 v^3$,

$$F_e = n_e \left(m_e / 2\pi T_e \right)^{3/2} \exp(-m_e v^2 / 2T_e)$$

is the electron’s Maxwellian velocity distribution, v is electron velocity, m_e is the electron mass, e is the electron charge, and n_e and T_e are the electron density and temperature, respectively. The BGK model is often simplified by using the thermal velocity in the collisional term ν_{ei} , but to improve its accuracy in these calculations, the velocity dependence was retained.³⁵ The standard collisionless results for the Thomson-scattering spectrum [Eq. (1)] are recovered in the limit of $\nu_{ei} = 0$ (Ref. 35).

Figure 156.37 shows the spectral width of EPW features, which is proportional to the EPW damping, for the collisionless, BGK, and VFP models. At a density of 10^{19} cm^{-3} , a damping minimum is obtained at 35 eV for both the VFP and BGK models. At electron temperatures >35 eV, the models converge because Landau damping dominates. The collisionless model, the standard for ideal plasma, works well at these temperatures. Collisional damping is important in calculating the width at temperatures below ~ 35 eV. This is consistent with the measurements, which indicated that a collisional theory was required to accurately interpret the spectra at these temperatures. Figure 156.37(b) compares the spectra calculated using the BGK and the VFP models, but without measurement effects. The BGK model is a good approximation for determining the resonant frequency, but it overestimates the width of the spectrum when collisions are important ($T_e \lesssim 35$ eV). This results in an overestimate of the electron temperature. The deviations from the VFP model reveal when improved theoretical interpretations of Thomson-scattering experiments are required.

In summary, limiting the pulse-front tilt in a spectrometer has allowed an ultrafast Thomson-scattering diagnostic to



E27749JR

Figure 156.37

(a) The width (FWHM) of the red-shifted EPW features is plotted for a density of 10^{19} cm^{-3} using the collisionless (red diamonds), BGK-collisional (blue squares), and VFP-collisional (green triangles) models as functions of electron temperature. (b) The spectrum calculated with the BGK model (dotted blue line) and VFP model (dashed green line) are shown for $T_e = 11 \text{ eV}$ and $n_e = 1.07 \times 10^{19} \text{ cm}^{-3}$. The BGK spectrum was multiplied by 1.8 to help illustrate the differences in width.

measure the plasma creation and picosecond evolution of the electron temperature and density in a laser-produced plasma. The measurements were compared with spectra calculated using the standard BGK model to account for collisions, showing that the BGK model overestimates the spectral width of the EPW features, leading to an overestimate of the electron temperature by up to $\sim 50\%$ at the most-collisional conditions. This overestimation of collisions by the BGK model has implications that extend well beyond Thomson scattering since this is an often-used collisional model in plasma physics, including modeling of thermal transport. These picosecond electron temperature and density measurements can be applied to laser-plasma devices that require knowledge of the rapidly evolving plasma conditions. Laser-plasma amplifiers require frequency matching between an electromagnetic beat wave and the plasma frequency for efficient energy transfer from a pump laser to the seed,⁴ but if the plasma frequency is rapidly evolving, as these experiments show, the amplifier will be detuned and the efficiency will be poor.^{38–42} With measurements of the plasma evolution, the system could be properly tuned to recover efficient energy transfer.

ACKNOWLEDGMENT

The work published here was supported by the U.S. Department of Energy Office of Fusion Energy Sciences under contract no. DE-SC0016253, the Department of Energy National Nuclear Security Administration under Award Number DE-NA0003856, the University of Rochester, and the New York State Energy Research and Development Authority.

REFERENCES

1. Y. Pin *et al.*, Phys. Rev. Lett. **92**, 175007 (2004).
2. J. Ren *et al.*, Nat. Phys. **3**, 732 (2007).
3. G. Vieux *et al.*, Sci. Rep. **7**, 2399 (2017).
4. V. M. Malkin, G. Shvets, and N. J. Fisch, Phys. Rev. Lett. **82**, 4448 (1999).
5. P. Michel, L. Divol, D. Turnbull, and J. D. Moody, Phys. Rev. Lett. **113**, 205001 (2014).
6. D. Turnbull, P. Michel, T. Chapman, E. Tubman, B. B. Pollock, C. Y. Chen, C. Goyon, J. S. Ross, L. Divol, N. Woolsey, and J. D. Moody, Phys. Rev. Lett. **116**, 205001 (2016).
7. D. J. Stark *et al.*, Phys. Rev. Lett. **115**, 025002 (2015).
8. D. Turnbull, C. Goyon, G. E. Kemp, B. B. Pollock, D. Mariscal, L. Divol, J. S. Ross, S. Patankar, J. D. Moody, and P. Michel, Phys. Rev. Lett. **118**, 015001 (2017).
9. K. Qu, Q. Jia, and N. J. Fisch, Phys. Rev. E **96**, 053207 (2017).
10. R. Bingham, Nature **394**, 617 (1998).
11. S. M. Hooker, Nat. Photonics **7**, 775 (2013).
12. S. C. Wilks, J. M. Dawson, and W. M. Mori, Phys. Rev. Lett. **61**, 337 (1988).
13. J. J. Rocca *et al.*, Phys. Rev. Lett. **73**, 2192 (1994); **75**, 1236(E) (1995).
14. A. Butler *et al.*, Phys. Rev. Lett. **91**, 205001 (2003).

15. K. Ta Phuoc *et al.*, Nat. Photonics **6**, 308 (2012).
16. N. D. Powers *et al.*, Nat. Photonics **8**, 28 (2014).
17. S. H. Glenzer *et al.*, Phys. Rev. Lett. **82**, 97 (1999).
18. D. S. Montgomery *et al.*, Laser Part. Beams **17**, 349 (1999).
19. J. L. Kline *et al.*, Phys. Rev. Lett. **94**, 175003 (2005).
20. C. Rousseaux *et al.*, Phys. Rev. Lett. **97**, 015001 (2006).
21. D. H. Froula, L. Divol, A. A. Offenberger, N. Meezan, T. Ao, G. Gregori, C. Niemann, D. Price, C. A. Smith, and S. H. Glenzer, Phys. Rev. Lett. **93**, 035001 (2004).
22. J. S. Ross, S. H. Glenzer, J. P. Palastro, B. B. Pollock, D. Price, G. R. Tynan, and D. H. Froula, Rev. Sci. Instrum. **81**, 10D523 (2010).
23. R. J. Henchen, M. Sherlock, W. Rozmus, J. Katz, D. Cao, J. P. Palastro, and D. H. Froula, Phys. Rev. Lett. **121**, 125001 (2018).
24. A. Visco, R. P. Drake, D. H. Froula, S. H. Glenzer, and B. B. Pollock, Rev. Sci. Instrum. **79**, 10F545 (2008).
25. S. C. Snyder, D. M. Crawford, and J. R. Fincke, Phys. Rev. E **61**, 1920 (2000).
26. G. Gregori *et al.*, Phys. Rev. E **65**, 046411 (2002).
27. B. B. L. Witte *et al.*, Phys. Rev. Lett. **118**, 225001 (2017).
28. W. Rozmus *et al.*, Astrophys. J. Suppl. Ser. **127**, 459 (2000).
29. G. Gregori and D. O. Gericke, Phys. Plasma **16**, 056306 (2009).
30. P. L. Bhatnagar, E. P. Gross, and M. Krook, Phys. Rev. **94**, 511 (1954).
31. M. Opher, G. J. Morales, and J. N. Leboeuf, Phys. Rev. E **66**, 016407 (2002).
32. W. Rozmus *et al.*, Phys. Rev. E **96**, 043207 (2017).
33. V. Bagnoud, I. A. Begishev, M. J. Guardalben, J. Puth, and J. D. Zuegel, Opt. Lett. **30**, 1843 (2005).
34. J. Katz, R. Boni, R. Rivlis, C. Muir, and D. H. Froula, Rev. Sci. Instrum. **87**, 11E535 (2016).
35. J. Sheffield, D. Froula, S. H. Glenzer, and N. C. Luhmann, Jr., *Plasma Scattering of Electromagnetic Radiation: Theory and Measurement Techniques*, 2nd ed. (Academic Press, New York, 2010).
36. A. V. Brantov, V. Yu. Bychenkov, and W. Rozmus, Phys. Rev. Lett. **108**, 205001 (2012).
37. V. Yu. Bychenkov, Plasma Phys. Rep. **24**, 801 (1998).
38. D. S. Clark and N. J. Fisch, Phys. Plasmas **10**, 3363 (2003).
39. R. L. Berger, D. S. Clark, A. A. Solodov, E. J. Valeo, and N. J. Fisch, Phys. Plasmas **11**, 1931 (2004).
40. J. P. Farmer, B. Ersfeld, and D. A. Jaroszynski, Phys. Plasmas **17**, 113301 (2010).
41. N. A. Yampolsky and N. J. Fisch, Phys. Plasmas **18**, 056711 (2011).
42. X. Yang *et al.*, Sci. Rep. **5**, 13333 (2015).